nature communications

Article

https://doi.org/10.1038/s41467-025-57569-0

Quantifying the distinct role of plasmon enhancement mechanisms in prototypical antenna-reactor photocatalysts

Received: 15 June 2024

Accepted: 25 February 2025

Published online: 06 March 2025

Check for updates

Shuang Liu[1,8], Zhiyi Wu[1,8], Zhijie Zhu[1,8], Kai Feng[1], Yuxuan Zhou[1], Xinge Hu[1], Xiong Huang[2], Binbin Zhang[3], Xudong Dong[1], Yueru Ma[1], Kaiqi Nie[4], Jiahui Shen[1], Zidi Wang[1], Jiari He[5], Jiaqi Wang[1], Yu Ji[1], Binhang Yan[4], Qingfeng Zhang[3], Alexander Genest[6], Xiaohong Zhang[1], Chaoran Li[1,7] ✉, Bo Wu[2], Xingda An[1] ✉, Günther Rupprechter[6] & Le He[1] ✉

Plasmonic photocatalysis enabled by the unique localized surface plasmon resonance represents a promising approach for efficient solar energy conversion. Elucidating the distinct plasmonic catalytic mechanisms and quantification of their effect is crucial yet highly challenging, due to their complex and synergistic nature. Herein, we achieve the differentiation and quantification of thermal as well as various non-thermal reaction mechanisms in prototypical Au-$[Fe(bpy)_3]^{2+}$ antenna-reactor photocatalysts using water splitting as test reaction. Through modification of the resonance condition and connection schemes, non-thermal plasmonic charge and energy transfer mechanisms are selectively shielded. It is found that plasmonic charge carrier-induced photochemistry dominates the photocurrent (~57%) in a reducing, hydrogen evolution environment; whereas resonant plasmonic energy transfer dominates (~54%) in an oxidative, oxygen evolution environment. Our approach provides generalized and fundamental understandings on the role of surface plasmons in photocatalysis as well as important design principles for plasmonic photocatalysts towards distinct reaction types and catalyst configurations.

Plasmonic photocatalysis represents an emerging sub-field of heterogeneous catalysis that can convert solar energy, one of the most abundant sustainable energy forms on earth, into chemical energy facilitated by nanoplasmonic catalysts[1,2]. Signified by the localized surface plasmon resonance (LSPR) effect, plasmonic nanostructures typically possess versatile optical response and photophysical properties that facilitate their distinct functionalities in catalytic pathways[3–6]. As a result, plasmonic catalysts, such as Au, Ag, or Cu nanoparticles, intricately designed non-noble plasmonic compounds, and plasmonic superstructures have been increasingly exploited in the catalytic conversion of CO_2[7,8], H_2O[9,10], urea[11], methanol[12,13] among others[14,15].

[1]Institute of Functional Nano & Soft Materials (FUNSOM) and Jiangsu Key Laboratory of Advanced Negative Carbon Technologies, Soochow University, Suzhou 215123, PR China. [2]Guangdong Provincial Key Laboratory of Optical Information Materials and Technology, Institute of Electronic Paper Displays, South China Academy of Advanced Optoelectronics, South China Normal University, Guangzhou 510006, PR China. [3]College of Chemistry and Molecular Sciences, Wuhan University, Wuhan, Hubei 430072, PR China. [4]Department of Chemical Engineering, Tsinghua University, Beijing 100084, China. [5]State Key Laboratory of Crystal Materials, Institute of Crystal Materials, Shandong University, Jinan, Shandong 250100, PR China. [6]Institute of Materials Chemistry, TU Wien, Wien, Austria. [7]Jiangsu Key Laboratory for Carbon-Based Functional Materials & Devices, Soochow University, Suzhou 215123 Jiangsu, PR China. [8]These authors contributed equally: Shuang Liu, Zhiyi Wu, Zhijie Zhu. ✉e-mail: crli@suda.edu.cn; xdan@suda.edu.cn; lehe@suda.edu.cn

Attaining in-depth understanding on the distinct plasmonic photocatalytic mechanisms is crucial for tuning the reaction conditions, pathways, and products; yet it is highly demanding due to their complex nature. Driven by the non-radiative relaxation of the localized surface plasmons, a number of distinct mechanisms could co-exist and, thus, simultaneously contribute to the catalytic processes[16,17]. For instance, the rapid dephasing of the plasmons through Landau damping and electron-electron scattering is able to induce the thermalization of ballistic "hot" charge carriers that directly participate in the catalytic pathways[6,18,19]; the intense resonant electromagnetic near-field (E-field) produced by the coherent oscillation of free electrons at nanoplasmonic surfaces could also sustain resonant energy transfer mechanisms[11,20,21]. Moreover, through electron-phonon scattering of the hot carriers, plasmonic photothermal effect could also be initiated for highly localized heating[22,23]. Intensive efforts have thus been made towards identifying the contributions of each distinct mechanism in plasmonic photocatalysis, particularly those of thermal versus non-thermal effects[1,24–26]. However, it remains highly challenging to distinguish and quantify thermal vs non-thermal contributions due to the inaccurate measurement of catalyst surface temperature, or amongst various non-thermal pathways because of the intricate synergies that occur between plasmonic charge and energy transfer mechanisms.

In this work, we have developed a generalized "selective shielding" strategy for identification and quantification of distinct plasmonic photocatalytic mechanisms, particularly amongst various non-thermal reaction pathways, employing a prototypical Au-$[Fe(bpy)_3]^{2+}$ plasmonic nanocatalyst and water splitting as test reaction. Through modifying the connection scheme from a conductive to an insulating layer, and adjusting the resonance conditions between the plasmonic antenna and the reactor component, the charge transport and energy transfer mechanisms were selectively shielded. In addition, thermal contributions were calibrated using in-situ Raman nano-thermometry. It was found that plasmonic charge carrier-mediated photoreduction dominates the photocurrent (~57%) in a reducing, hydrogen evolution environment; whereas resonant plasmonic energy transfer dominates (~54%) in an oxidative, oxygen evolution environment. Our work provides in-depth understandings on the role of plasmon resonance in photocatalysis as well as important design principles for plasmonic photocatalysts towards distinct types of chemical reactions.

Results

Design and characterization of the Au-$[Fe(bpy)_3]^{2+}$ Plasmonic Nanocatalyst

The primordial plasmonic photocatalyst configuration typically involves the use of plasmonic nanoparticles (NPs) as nanoantenna and active catalyst components as the reactors[27–29]. A prototypical plasmonic antenna-reactor (A-R) nanocatalyst was first constructed using Au NP cores (Figs. S1a, b) as nanoantenna and tris(2,2′-bipyridine)iron(II) ($[Fe(bpy)_3]^{2+}$) (Fig. S1c) as the catalytic component, whose intramolecular metal-to-ligand charge transfer (MLCT) absorption feature at 520–550 nm (Fig. S1d) overlaps spectrally with the LSPR frequency of Au NPs to guarantee efficient resonant enhancement[4,30]. The intermediate size of the Au nanoantenna used in the nanocatalyst (59.56 ± 7.07 nm) effectively balances the radiative *vs* dissipative plasmonic energy losses, and potentially enables both plasmonic charge and energy transfer-mediated non-thermal photocatalytic mechanisms[11,31]. To enable the differentiation of distinct photophysical mechanisms, two different connection schemes between the antenna and reactor components were utilized, including (a) via a thiolated polyethylene glycol (PEG) linker with carboxyl end groups (HS-PEG-COOH, $M_w = 456$) (denoted as Au-$[Fe(bpy)_3]^{2+}$), which has been reported to facilitate the transport of plasmonic charge carriers[11]; and (b) via a silica nanoshell of comparable thickness (denoted as $Au@SiO_2$-$[Fe(bpy)_3]^{2+}$), which insulates the charge transfer processes and enables only the resonant field-enhancement[16,30] (Fig. 1a). In the Au-$[Fe(bpy)_3]^{2+}$ nanocatalyst, the thiol moieties at the thiolated end of the linker covalently binds to Au[32,33], while the ionized -COO^- at the other end connects with $[Fe(bpy)_3]^{2+}$ molecules primarily through electrostatic interaction[34], as indicated by our Zeta potential measurements (Table S1). In addition, moderate van der Waals (VDW) interactions between the non-polar bipyridine ligands and the alkyl chain in the linker is also present[11] (Fig. S2), contributing to the pinning of the $[Fe(bpy)_3]^{2+}$ catalyst at the tip of the linker molecules (Fig. S3a). Similarly, the silane moieties on the $Au@SiO_2$ surface as well as the hydrophobic silica surface sustains electrostatic as well as moderate VDW interactions that collectively integrates the $[Fe(bpy)_3]^{2+}$ molecules[35,36] (Fig. S3b).

The Au-$[Fe(bpy)_3]^{2+}$ plasmonic photocatalyst was next used for structural and photophysical characterization. Transmission electron microscopy (TEM) was first used to evidence its successful preparation. A distinct layer of the thiolated PEG-COOH linker with a thickness of ~2.5 nm could be observed around the Au nanoantenna (Fig. 1b), which is consistent with the contour length of HS-PEG-COOH at corresponding molecular weights[37]. In proof of successful $[Fe(bpy)_3]^{2+}$ binding, Au and Fe elements were mapped across an individual nanoparticle by Energy-Dispersive X-Ray Spectroscopy (EDS) in scanning TEM (STEM) mode (Fig. 1c). The distribution of the two elements shows them to co-localize within the boundary of the particle, but with Fe preferentially residing at the perimeter. Moreover, spectroscopic characterization provides further evidence on the successful formation of Au-$[Fe(bpy)_3]^{2+}$. The Raman spectrum of Au-$[Fe(bpy)_3]^{2+}$ displays signature peaks both of $[Fe(bpy)_3](PF_6)_2$ (1322, 1492, 1608 cm^{-1} etc.)[38] and Au NPs (1448 cm^{-1} corresponding to the surface ligands[39]) (Fig. 1d). Further Raman mapping at 1448 cm^{-1} (Au) and 1492 cm^{-1} ($[Fe(bpy)_3]^{2+}$) demonstrates the overlapping distribution of the two components (Fig. 1d, insets). In our X-ray photoelectron spectroscopy (XPS) measurements, the Au 4 f characteristic peaks of the Au-$[Fe(bpy)_3]^{2+}$ nanocatalysts and those of Au nanoparticles show significant differences (Figs. 1e and Fig. S4). In addition to the Au^0 features (87.0 and 83.4 eV), Au-$[Fe(bpy)_3]^{2+}$ exhibits a distinct set of peaks at high energies (88.8 and 84.8 eV) attributed to the $Au^{1+}4f_{7/2}$ and $4f_{5/2}$ peaks derived from the covalent bonding of the thiolated Au atoms on the surface of the nanoantenna, with the extent of the shifts highly consistent with previous reports[40,41]. In summary, all results confirm the successful formation of the Au-$[Fe(bpy)_3]^{2+}$ nanocomposite.

As a result of the resonance between Au LSPR and $[Fe(bpy)_3]^{2+}$ intramolecular MLCT transition, an evident increase in the absorbance of the Au-$[Fe(bpy)_3]^{2+}$ nanocatalyst is observed in the range of 450–550 nm, which surpasses that of the Au colloids and $[Fe(bpy)_3]^{2+}$ combined, as well as that of a physical mixture of the two components at identical concentrations (Fig. 1f). Notably, the absorbance of Au-$[Fe(bpy)_3]^{2+}$ almost doubled compared to $[Fe(bpy)_3]^{2+}$ at the absorbance maximum of 524 nm, after the absorbance of Au colloids was subtracted. This phenomenon evidences the resonant, synergistic enhancement in absorbance through plasmon-mediated energy transfer[11,42]. Based on the light extinction behavior, we have also optimized the amount of $[Fe(bpy)_3]^{2+}$ in the hybrid nanocomposite. With an increasing amount of $[Fe(bpy)_3]^{2+}$ (5.65 mM), the absorbance of corresponding Au-$[Fe(bpy)_3]^{2+}$ also exhibited a gradual increase until an input amount of 150 μl, when the increase showed an evident halt (Fig. S5a). This suggests that the binding capability of the linker on the Au surface has reached saturation, and is consistent with dynamic light scattering (DLS) results (Fig. S5b), where a higher input of $[Fe(bpy)_3]^{2+}$ than 150 μl led to evident particle aggregation due to neutralization of the negative charges from $[Fe(bpy)_3]^{2+}$ binding, lowering the electrostatic repulsion between monodispersed nanocomposites. Thus, an optimized Fe concentration of 12.56 ± 2.10 ppm in Au-$[Fe(bpy)_3]^{2+}$ colloid was obtained was chosen for the following characterizations (Table S2).

https://doi.org/10.1038/s41467-025-57569-0

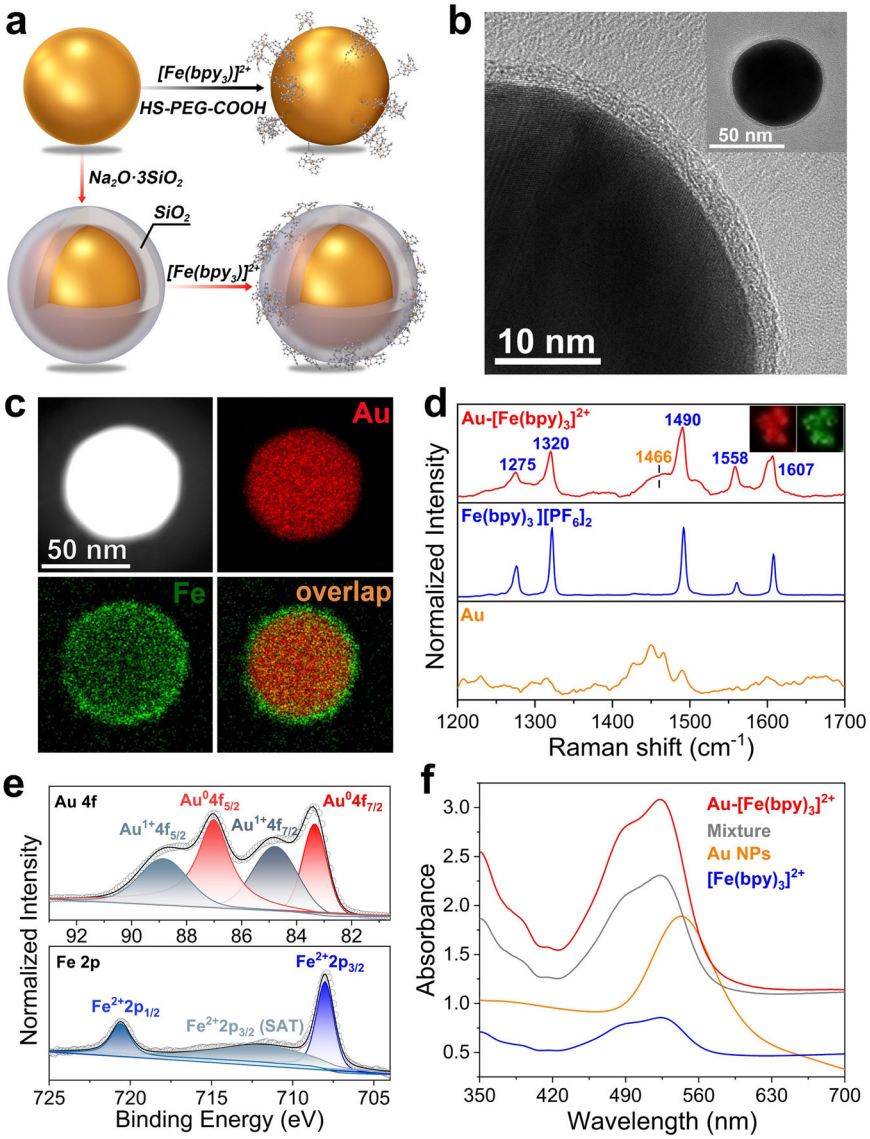

Fig. 1 | Design of the Au-$[Fe(bpy)_3]^{2+}$ plasmonic nanocatalyst. a Synthesis of Au-$[Fe(bpy)_3]^{2+}$ with different connection schemes. **b** TEM images and (**c**) STEM image and EDS elemental mappings of Au-$[Fe(bpy)_3]^{2+}$ nanocomposite. **d** Raman spectra of Au-$[Fe(bpy)_3]^{2+}$ and controls under 633 nm incident laser. Insets: Raman mapping at 1448 (red) and 1492 (green) cm^{-1}. **e** Au *4f* and Fe *2p* XPS spectra and fitting. **f** UV-vis absorbance spectra of Au-$[Fe(bpy)_3]^{2+}$ colloid and controls.

Identification of the Resonant Plasmonic Energy and Charge Transfer Mechanisms

Plasmonic near field-mediated resonant energy transfer and hot carrier transport are two plausible mechanisms of plasmon-enhancement associated with the Au-$[Fe(bpy)_3]^{2+}$ nanocomposites[30,43,44]. To identify the resonant energy transfers, Finite-difference time-domain (FDTD) simulations of the E-field around a single Au NP were first performed. Upon resonant illumination, noticeable enhancement of the E-field occurs in a region within 10 nm around the particle (Fig. 2a, inset). To provide experimental evidence on the effect of the resonant electromagnetic near-field, we compared the absorbance spectrum (ABS) and the single-particle dark-field scattering (SCA) spectrum of the Au-$[Fe(bpy)_3]^{2+}$ nanocomposite as well as a Au nanoparticle only control (Figs. 2a, see also Fig. S6). Both scattering spectra showed a redshift of the scattering maxima compared to the absorbance spectrum due to the increased refractive index on the substrate. Notably, the SCA peak position of Au-$[Fe(bpy)_3]^{2+}$ demonstrates an evident redshift by 12 nm compared to Au single particles, which suggests effective dampening of the Au plasmons through resonant energy transfer from Au into $[Fe(bpy)_3]^{2+}$ [45,46]. It could also be observed that the SCA full width at half maxima (FWHM) of Au-$[Fe(bpy)_3]^{2+}$ (93.17 nm) is evidently larger than that of Au NPs control (79.34 nm), which could also be attributed to the energy loss of Au plasmons[47,48], and further corroborate the above energy transfer pathway in Au-$[Fe(bpy)_3]^{2+}$ nanocomposite. In addition, steady-state photoluminescence (PL) spectra of Au-$[Fe(bpy)_3]^{2+}$ and controls demonstrate significant changes to the emission pattern (Fig. S7), consistent with the resonant energy transfer from Au towards $[Fe(bpy)_3]^{2+}$ that promotes the photoexcited state energy of the latter[49–51].

The generation and transfer of plasmonic hot charge carriers could also be an important factor in the Au-$[Fe(bpy)_3]^{2+}$ nanocatalyst. This is supported by our simulations of the charge distribution profiles of Au-$[Fe(bpy)_3]^{2+}$, where the presence of distinct electric potentials is found within the Au, linker, and $[Fe(bpy)_3]^{2+}$ layers (Fig. S8). In-situ X-Ray Absorption Fine Structures (XAFS) spectroscopy and in-situ irradiated XPS (ISI-XPS) provide direct experimental evidence for the plasmonic charge transfer from Au nanoantenna towards the $[Fe(bpy)_3]^{2+}$ catalyst. When Au-$[Fe(bpy)_3]^{2+}$ was exposed to 550 nm monochromic illumination corresponding to the red-edge of the Au LSPR absorption band (552 nm) (Fig. S9), the in-situ X-Ray Absorption Near-Edge (XANES) spectra of the Fe rising edge demonstrates an

https://doi.org/10.1038/s41467-025-57569-0

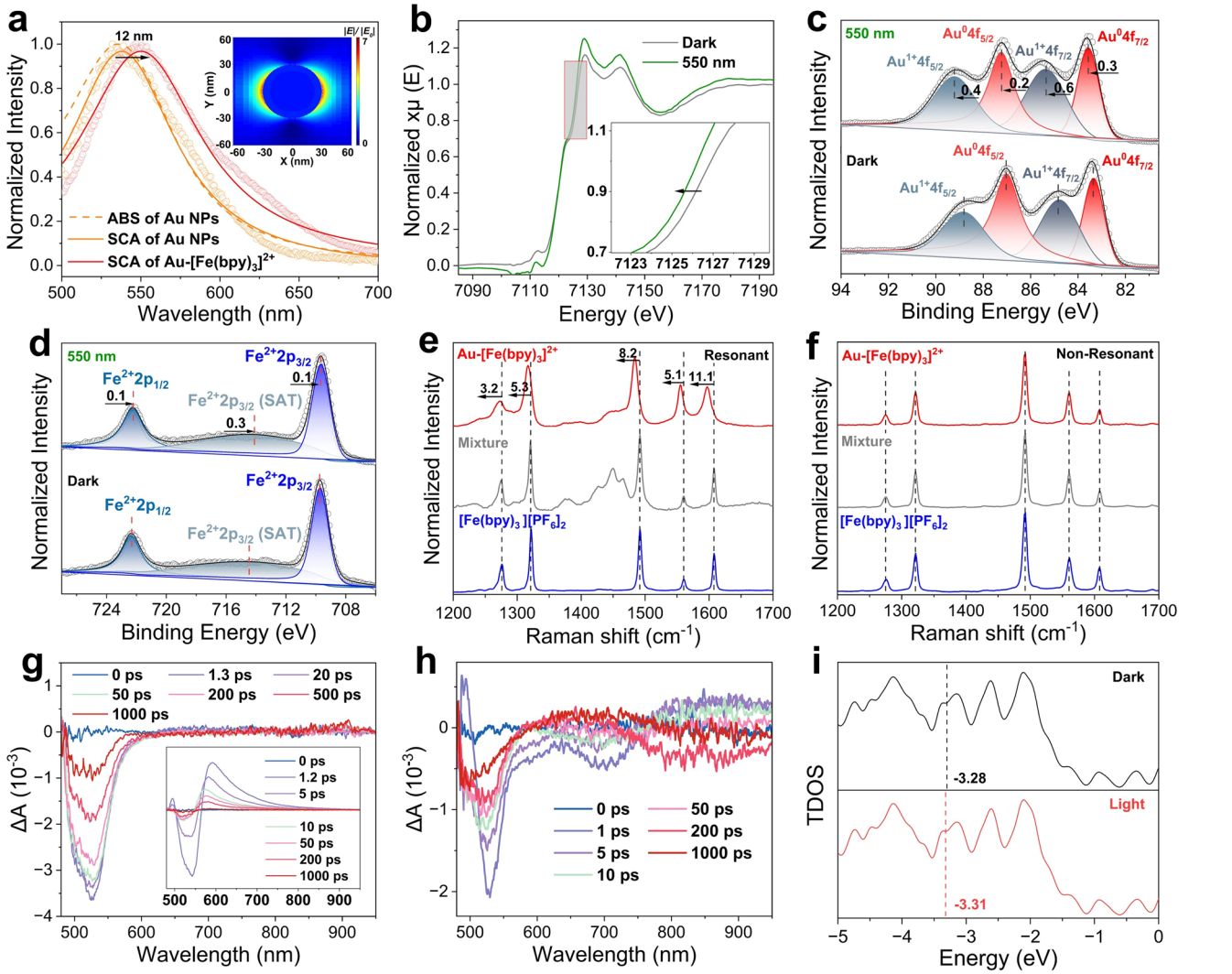

Fig. 2 | Characterization of Plasmonic Energy and Charge Transfer Mechanisms. **a** Absorbance spectra (ABS) of Au NPs and single-nanoparticle scattering spectra (SCA) of Au NPs and Au-$[Fe(bpy)_3]^{2+}$. Inset: Simulated E-field around a single Au NP. **b** Fe K-edge XANES of Au-$[Fe(bpy)_3]^{2+}$ in dark or under 550-nm illumination. **c** Au *4f* and (**d**) Fe *2p* XPS spectra and fittings of Au-$[Fe(bpy)_3]^{2+}$ in dark or under 550-nm illumination. **e**, **f** Raman spectra of Au-$[Fe(bpy)_3]^{2+}$ and controls with resonant (**e**) and non-resonant incident wavelengths (**f**). **g**, **h** TA spectra of the $[Fe(bpy)_3]^{2+}$ solution (**g**), of Au NP colloid (**g**, inset), and of Au-$[Fe(bpy)_3]^{2+}$ (**h**) with pump wavelength of 515 nm. **i** DFT calculations of the density of electromagnetic states of Au-$[Fe(bpy)_3]^{2+}$ with and without illumination.

apparent shift towards lower energies compared to without illumination (Fig. 2b), while the Fe-N bond manifested slight elongation (Fig. S10a). Furthermore, with illumination, the Au *4f* XPS bands in the Au-$[Fe(bpy)_3]^{2+}$ nanocatalyst also demonstrate evident shifts towards higher binding energies (Fig. 2c). In particular, the Au^{1+} features exhibit more significant shifts due to the bridging role of the surface Au-thiol moiety in plasmonic charge transfer. On the other hand, the Fe *2p* peaks in Au-$[Fe(bpy)_3]^{2+}$ shifted towards lower binding energies (Fig. 2d). This opposite shift of Au and Fe signatures was also observed for Au-$[Fe(bpy)_3]^{2+}$ upon broad-band irradiation (Figs. S10b, c), but was not seen for Au NP-only and $[Fe(bpy)_3]^{2+}$-only controls (Fig. S11). These results are highly consistent with the light-induced plasmonic charge transfer from Au towards $[Fe(bpy)_3]^{2+}$.

Analysis of the PL and Raman spectra of Au-$[Fe(bpy)_3]^{2+}$ and controls provides further experimental evidence on the transfer of plasmonic charge carriers. Significantly reduced PL intensity was observed for Au-$[Fe(bpy)_3]^{2+}$ compared to the free-standing $[Fe(bpy)_3]^{2+}$-only and the physical mixture controls (Fig. S12). In addition, Au-$[Fe(bpy)_3]^{2+}$ had a longer lifetime (τ_1 = 312 ps) than $[Fe(bpy)_3]^{2+}$ solution (τ_1 = 173 ps) as well as the control mixture (τ_1 = 243 ps) (Fig. S13). The reduction in PL intensity, combined with the prolonged lifetime, demonstrated effective separation and transport of charge carriers in Au-$[Fe(bpy)_3]^{2+}$ [52]. Furthermore, in surface-enhanced Raman spectroscopy (SERS) measurements, with resonant excitation of the drop-casted thin film (Fig. S14), the signature peaks of $[Fe(bpy)_3]^{2+}$ in Au-$[Fe(bpy)_3]^{2+}$ showed apparent shifts towards lower frequencies compared to freestanding $[Fe(bpy)_3]^{2+}$ (Fig. 2e), which was not observed with non-resonant irradiation conditions (Figs. 2f and Fig. S15). This observation indicates lengthening of the Fe-N bonds and decreases in its stretching frequencies due to charge injection from Au nanoantenna under resonant illumination [53], and is highly consistent with our XANES analyses above.

To characterize the dynamics of the photophysical responses following photoexcitation, transient absorption (TA) spectroscopy was next performed. TA spectra of $[Fe(bpy)_3]^{2+}$ and Au NP-only controls respectively exhibits excitonic band bleaching centered at around 525 nm (Fig. 2g) and LSPR bleaching with photo-induced absorption bands on both sides, typical of hot carrier-induced plasmon broadening (Fig. 2g, inset). The overlap between both features led to an evident bleaching band between 500 nm-550 nm for Au-$[Fe(bpy)_3]^{2+}$ (Fig. 2h). Bi-exponential decay fitting of the kinetic traces for Au-$[Fe(bpy)_3]^{2+}$ at 525 nm reveals a short lifetime τ_1 = 3.1 ps and a

longer component τ_2 = 680.2 ps (Fig. S16). τ_1 is similar to that found for Au NPs (2.9 ps) and is attributed to hot carrier relaxation by electron-phonon (e-ph) scattering, while τ_2 is contributed both by the exciton bleaching lifetime of $[Fe(bpy)_3]^{2+}$ (928.6 ps) and phonon-phonon (ph-ph) scattering lifetime in Au NP only solution (567.0 ps)[54,55]. Intriguingly, after resonant pump excitations of the Au-$[Fe(bpy)_3]^{2+}$ nanocatalyst, new absorption features were observed at ~700 nm and ~850 nm (Fig. 2h), which are not seen in the Au NP-only and $[Fe(bpy)_3]^{2+}$-only controls. These bands are highly consistent with those found previously for triplet and quintet excited states of $[Fe(bpy)_3]^{2+}$ [50]. Close examination and fittings for the latter show a slow buildup with a time constant of around 35 ps and a decay lifetime as long as 1.2 ± 0.3 ns (Fig. S17). The decay lifetime is consistent with the excitonic lifetime found for $[Fe(bpy)_3]^{2+}$, confirming its origin from $[Fe(bpy)_3]^{2+}$ rather than Au NPs. The slow buildup of the photoexcited states is in contradict to the ultrafast populating (<50 fs) by direct photoexcitation[50], thus evidencing the significant role of resonant plasmonic energy and charge transfers in bleaching of the triplet and quintet states.

To gain deeper insights on the electronic structure of the Au-$[Fe(bpy)_3]^{2+}$ nanocatalyst, density-functional theory (DFT) calculations were next performed. From our density of electromagnetic (DOS) calculations, the d-band centers of Au-$[Fe(bpy)_3]^{2+}$ downshifted under light illumination (Fig. 2i). The surface electronic spin density of the $[Fe(bpy)_3]^{2+}$ molecule was significantly elevated under light irradiation (Fig. S18a), which is consistent with the charge transfer behavior from Au towards $[Fe(bpy)_3]^{2+}$. In addition, the Fermi energy level of Au NPs is higher compared to the calculated LUMO of the catalyst molecule, which presents possibility of plasmonic charge carrier transfer from Au towards $[Fe(bpy)_3]^{2+}$ that could be further promoted by resonant photoexcitation into higher-temperature Fermi-Dirac distribution (Fig. S18b). Overall, these experimental and computational findings provide direct evidence on the occurrence of both resonant plasmonic near-field-mediated energy transfer and plasmonic hot carrier transfer from the Au nanoantenna to $[Fe(bpy)_3]^{2+}$ upon resonant illumination.

Plasmonic catalytic performance and mechanisms

The resonant plasmonic charge and energy transfer mechanisms described above are likely to provide the Au-$[Fe(bpy)_3]^{2+}$ nanocatalyst with favorable photoelectrochemical potential and plasmonic photocatalytic performance[14,15,56,57]. In this context, we probed its catalytic performance using the water splitting half reactions, hydrogen and oxygen evolution, as test reactions that respectively provide a reductive and oxidative environment. Notably, due to the redox capability of the Fe(II) center in $[Fe(bpy)_3]^{2+}$ via both reductive (Reaction (1)) and oxidative (Reaction (2)) conversions[11], it possesses great potentials to facilitate both reductive and oxidative half reactions (Fig. S19), promising overall water splitting photocatalysis.

$$\left[Fe(bpy)_3\right]^{2+} + 1e^- \rightleftharpoons \left[Fe(bpy)_3\right]^{1+} \quad (1)$$

$$\left[Fe(bpy)_3\right]^{2+} \rightleftharpoons \left[Fe(bpy)_3\right]^{3+} + 1e^- \quad (2)$$

The catalytic performance was first characterized in 0.05 M H_2SO_4 towards hydrogen evolution (Fig. 3). In linear scanning voltammetry (LSV) measurements (Fig. 3a), Au-$[Fe(bpy)_3]^{2+}$ demonstrated high current density (−194.47 mA/cm^2) as well as strong light response. As an indicator of the photocatalytic performance, a photocurrent density (J_{photo}) of −120.92 mA/cm^2 was obtained with 520 nm light-emitting diode (LED) irradiation (100 mW/cm^2), close to the LSPR wavelength of Au NPs. Broad-band Xe lamp irradiation was also able to induce significant photoelectrochemical response, although to a lower extent than the resonant LED due to the wavelength-specific LSPR excitation. In contrast, control groups including Au NPs, $[Fe(bpy)_3]^{2+}$ solution at identical concentrations, and a physical mixture of both components failed to produce comparable photocatalytic activity due to the absence in the plasmon-mediated photophysical pathways. Au-$[Fe(bpy)_3]^{2+}$ demonstrated much lower Tafel slopes upon irradiation as compared to in dark or control groups under identical illumination (Fig. 3b). A decrease in reaction onset potential was also seen for Au-$[Fe(bpy)_3]^{2+}$ under irradiation (−0.4 V vs Ag/AgCl), which evidences the promising photocatalytic potential of the plasmonic nanocatalysts[19,58]. Chronoamperometric I-t curves obtained with a constant applied bias of −0.8 V demonstrated much higher photocurrent for Au-$[Fe(bpy)_3]^{2+}$, consistent with LSV and Tafel slope results (Fig. 3c).

Hydrogen production from the Au-$[Fe(bpy)_3]^{2+}$ nanocatalyst was next measured under photocatalytic and photoelectrochemical catalytic conditions. Upon Xenon light illumination (without applied bias), the Au-$[Fe(bpy)_3]^{2+}$ catalyst demonstrated a stable photocurrent density for hydrogen evolution (>200 μA/cm^2) over an extended period (Fig. S20a). H_2 product measurement under pure photocatalytic conditions shows that a maximum production rate and quantum efficiency of 0.70 μmol g^{-1} h^{-1} and 0.047% were reached at 2-hour (Fig. S20b), indicative of the favorable photocatalytic efficacy of the Au-$[Fe(bpy)_3]^{2+}$ nanocatalyst. For photoelectrochemical catalytic conditions under a constant applied bias of −0.8 V, an average HER rate of 2133.55 mmol g^{-1} h^{-1} was observed without irradiation (Fig. S21a). The average hydrogen production rate significantly increased to 4160.40 mmol g^{-1} h^{-1} with Xe light and 5194.02 mmol g^{-1} h^{-1} with 550 nm illumination at 1-sun intensity (Figs. 3d and Fig. S21b). Under both irradiation conditions, the hydrogen production rate gradually increased due to the photothermal effect. In particular, a highest hydrogen production rate of 6379.02 mmol g^{-1} h^{-1} was obtained under 550 nm light irradiation in 8 cycles, demonstrating the great potential and stability of the Au-$[Fe(bpy)_3]^{2+}$ nanocatalyst in plasmonic photoelectrocatalysis.

To substantiate the catalyst's stability, we quantified the Au and Fe elemental compositions in the nanocatalyst before and after photoelectrocatalytic measurements, where only a slight decrease in the relative Fe content was observed in the collected catalyst after reaction (Table S3), suggesting that $[Fe(bpy)_3]^{2+}$ is stably anchored during catalysis. The XRD patterns, TEM images and XPS spectra of the Au-$[Fe(bpy)_3]^{2+}$ catalyst, both before and after the reaction, show almost no detectable changes. In particular, in the TEM images for the nanocatalyst after reaction, the HS-PEG-COOH layer was still observed around the Au NP, suggesting the structural integrity of the nanocatalyst (Fig. S22). No change in the Fe valence state was observed in the Fe *2p* XPS spectra before and after reaction (Fig. S23). In addition, in-situ Raman spectroscopy of the nanocatalyst measured in identical conditions as in the PEC measurements also show negligible changes to the vibration signatures over a period of 5 h (Fig. S24). These findings collectively attest to the remarkable stability of the catalyst during prolonged catalytic tests. To obtain further understandings of the photocatalytic performance of Au-$[Fe(bpy)_3]^{2+}$, LSV curves were also obtained in a 0.1 M NaOH electrolyte to assess the oxygen evolution capability. Interestingly, a trend opposite to that in hydrogen evolution was observed. Au-$[Fe(bpy)_3]^{2+}$ demonstrated lower current density and later onset potential upon irradiation as compared to in dark (Fig. S25a). This may be due to the negative role of plasmonic hot electrons in oxidative environment[30,59]. Chronoamperometric I-t curves indicate steady catalytic performance of Au-$[Fe(bpy)_3]^{2+}$ for up to 10 h (Fig. S25b).

To elucidate the plasmon enhancement mechanisms in hydrogen evolution, we first performed light-modulated photocurrent response measurements with polychromic Xenon lamp or 520 nm and 550 nm LEDs. The modulated photocurrents were recorded in consecutive light-on/light-off cycles under different external biases (−0.2 V and −0.05 V). As shown in Figs. 3e and Fig. S26, the light-modulated photocurrent response in both conditions clearly exhibited two distinct regions: a rapid response current (I_{RC}) region and a

https://doi.org/10.1038/s41467-025-57569-0

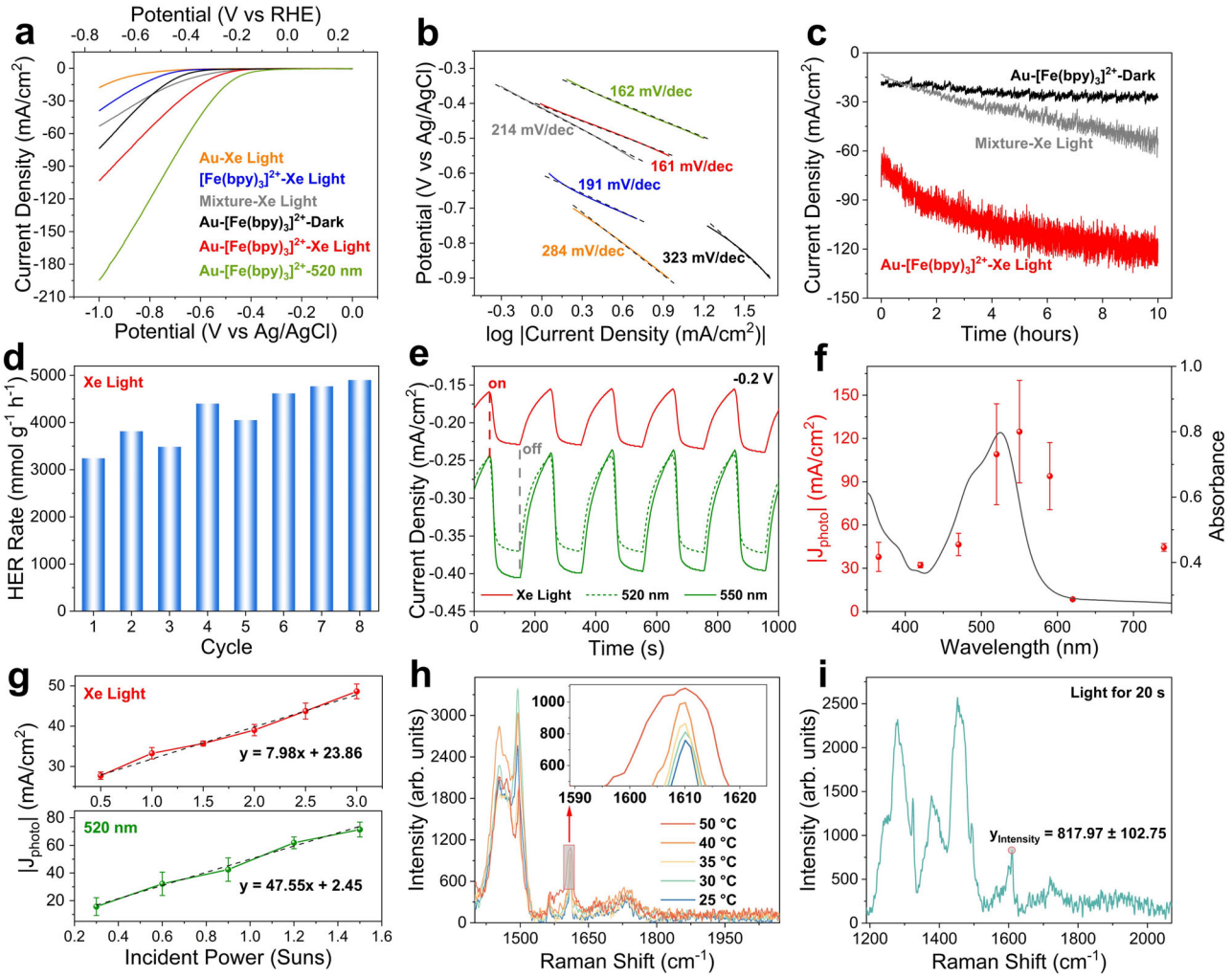

Fig. 3 | Plasmon-Mediated Catalytic Performance and Mechanism. a LSV curves, (**b**) Tafel slopes, and (**c**) chronoamperometric I-t curves at −0.8 V (vs Ag/AgCl) for Au-$[Fe(bpy)_3]^{2+}$ and controls in dark or with irradiation. **d** Photoelectrochemical hydrogen production of Au-$[Fe(bpy)_3]^{2+}$ under Xe light irradiation at −0.8 V. **e** Light-modulated photocurrent measured with an applied bias of −0.2 V with or without illumination at 100 mW/cm². **f** Wavelength dependence of Au-$[Fe(bpy)_3]^{2+}$ catalytic J_{photo} compared to its absorbance. **g** Plot of Au-$[Fe(bpy)_3]^{2+}$ J_{photo} as a function of incident light power. **h**, **i** Raman nano-thermometry spectra of Au-$[Fe(bpy)_3]^{2+}$ at different temperatures (**h**) or after irradiation for 20 seconds (100 mW/cm²) (**i**). Error bars in all figures represent standard deviations of three independent measurements.

subsequent slow-response current (I_{SC}) region, which indicates the presence of both non-thermal and thermal effects and is consistent with previous observations[60,61]. The proportion of I_{RC} owing to non-thermal photochemical effect is evidently larger, indicating a non-thermal effect-dominating process. Notably, both the J_{photo} and the proportion and of I_{RC} was larger with 550 nm illumination, which corresponds to the plasmonic red-edge. The duration of I_{RC} varied in comparison with previous reports, likely due to the prolonged carrier lifetimes and the occurrence of resonant energy transfer-mediated photoreactivity[55,62,63]. Fitting of the dependence of photocurrent density on light modulation frequencies shows a non-linear dependence (Fig. S27), which is also consistent with the dominance of photochemical effects[54].

To further demonstrate the non-thermal enhancement pathways in the Au-$[Fe(bpy)_3]^{2+}$ nanocatalyst, we assessed the dependence of photocatalytic properties on irradiation wavelength and intensity. The photocurrent densities of Au-$[Fe(bpy)_3]^{2+}$ were obtained with irradiation at different wavelengths (all at 1-sun) (Fig. 3f). In general, the dependence profile of J_{photo} on incident wavelength closely resembles the absorbance spectrum of Au-$[Fe(bpy)_3]^{2+}$, with only a slight redshift due to the aggregation of the nanocomposites on the electrode surfaces. Radiation at the red-edge of the Au plasmons (550 nm) led to the highest J_{photo} (−124.71 ± 35.53 mA/cm²). In terms of the dependence of photocatalytic performance on irradiation light power, it has been previously reported that a linear relationship is typically associated with non-thermal photochemical effect-dominated pathways, whereas a super-linear relationship indicates photothermal effect-induced pathways[17,64,65]. Notably, the J_{photo} obtained by both the 520 nm LED ($y = 47.55x + 2.45$, $R^2 = 0.99$) and the Xe lamp ($y = 7.98x + 23.86$, $R^2 = 0.99$) up to 300 mW/cm² showed a linear dependence on the incident light intensity (Fig. 3g), consistent with a non-thermal effect-dominated reaction pathway largely driven by plasmonic hot carrier transfer as a result of desorption induced by electronic transition (DIET) pathway[66].

To investigate the influence of the photothermal effect, we first used an infrared (IR) camera and thermocouple to measure the temperature change at the electrode surface or in the electrolyte for Au-$[Fe(bpy)_3]^{2+}$ during the catalytic process. Under 1-sun irradiation, both measurements showed only a moderate change in temperature ($\Delta T < 2$ °C) (Fig. S28). As these macroscopic temperature measurement results can only reflect the average temperature in the catalytic macro-environment, in-situ Raman nano-thermometry was next exploited for

the precise characterization of the surface temperature on the Au-$[Fe(bpy)_3]^{2+}$ nanocatalyst (Fig. 3h). Raman nano-thermometry was performed with in situ illumination based on the temperature-sensitive behavior of the vibrational modes in $[Fe(bpy)_3]^{2+}$ [67], and the precise temperature was calibrated through external heating. As expected, the peak intensity of the $[Fe(bpy)_3]^{2+}$ lattice vibration (~1610 cm^{-1}) scales linearly with temperature (Fig. S29a). To investigate the effect of photothermal conversion, 1-sun Xe-lamp illumination was applied for varying durations (Fig. S29b). The peak intensity increased evidently with increasing illumination times, and the temperature corresponding to the peak intensity after 20 seconds of illumination (which corresponds to the LSV scanning time) can be calculated via linear fitting (Fig. 3i). A surface temperature of 29.73 °C ($\Delta T \approx 5$ °C) was thus measured, comparable to recent reports using similar conditions[67]. Although the temporal resolution of the Raman nano-thermometry might be insufficient to capture the entire transient processes preceding plasmonic heating, in-situ Raman nano-thermometry is highly relevant to catalytic measurements, as it precisely measures the temperature change at the catalytic active sites. The influence of such electrolyte temperature changes on the catalytic performance was next evaluated by comparing the LSV curves for Au-$[Fe(bpy)_3]^{2+}$ in dark at different temperatures (Fig. S30). Moderate changes to the current densities were observed for Au-$[Fe(bpy)_3]^{2+}$ at temperatures up to 5 °C higher than room temperature. Overall, these results further confirm that the photothermal effect has not contributed significantly to the photocatalytic performance.

Differentiation and quantification of distinct plasmonic photocatalytic mechanisms

Based on the analyses above, it can be determined that the photocatalytic performance of the plasmonic nanocatalyst includes contributions from the following factors: (i) plasmonic charge carrier-induced photochemistry; (ii) resonant energy transfer-induced catalysis mediated by the plasmonic near field; (iii) synergistic effect between (i) and (ii) through resonant field-mediated charge transfer; (iv) the intrinsic photocatalytic performance of $[Fe(bpy)_3]^{2+}$; and (v) moderate contributions from photothermal effect. To differentiate the distinct catalytic mechanisms, particularly the plasmonic charge and energy transfers (mechanisms (i)-(iii)), we next modified the connection route of Au-$[Fe(bpy)_3]^{2+}$ from a conductive to an insulating layer, and adjusted the resonance conditions between the nanoantenna and the reactor component. Importantly, these modifications allow us to selectively shield the charge transport and resonant energy transfer mechanisms, respectively, in the plasmonic nanocatalyst.

To shield the effect of plasmonic charge transfer, we replaced the thiolated PEG-COOH linker in Au-$[Fe(bpy)_3]^{2+}$ with an insulating SiO_2 nanoshell (Au@SiO_2-$[Fe(bpy)_3]^{2+}$), which possess very similar thickness (~2.5 nm) to the contour length of the linker (Fig. 4). FDTD simulation of the E-field around a single Au@SiO_2-$[Fe(bpy)_3]^{2+}$ particle indicated an almost identical field intensity distribution as compared to Au-$[Fe(bpy)_3]^{2+}$ (Fig. S31). Thus, the change in connection type does not affect the resonant field-mediated energy transfer efficiency. TEM and EDS elemental mappings confirm the successful preparation of Au@SiO_2-$[Fe(bpy)_3]^{2+}$ (Fig. 4a, b). Notably, Au 4 f *ISI*-XPS spectra of Au@SiO_2-$[Fe(bpy)_3]^{2+}$ exhibit no evident changes of the Au binding energies under broad-band irradiation compared to in dark (Fig. 4c). Similarly, no evident shifts of the characteristic Raman peaks of Au@SiO_2-$[Fe(bpy)_3]^{2+}$ could be observed when compared to $[Fe(bpy)_3]^{2+}$ under resonant irradiation (Fig. 4d, see also Fig. S32). Moreover, the charge distribution simulation of Au@SiO_2-$[Fe(bpy)_3]^{2+}$ also indicates an absence of electric potential in the outermost $[Fe(bpy)_3]^{2+}$ layer due to charge transfer (Fig. S33). These observations are in distinct contrast to Au-$[Fe(bpy)_3]^{2+}$, and are indicative of the exclusion of plasmonic hot carrier transfer from Au nanoantenna to $[Fe(bpy)_3]^{2+}$. The catalytic performance of Au@SiO_2-$[Fe(bpy)_3]^{2+}$ was next measured. As expected, much reduced photocurrent ($J_{photo} = -2.79$ mA/cm^2) were observed with Xe lamp illumination compared to Au-$[Fe(bpy)_3]^{2+}$ ($J_{photo} = -33.26$ mA/cm^2) due to the exclusion of plasmonic charge carriers-induced photochemistry (Fig. 4e). The hindered charge transfer kinetics was further evidenced by electrochemical impedance spectroscopy (EIS) and Mott-Schottky measurements[55,68], where a much larger charge transfer resistance (R_{ct}) as well as reduced carrier mobility was measured for Au@SiO_2-$[Fe(bpy)_3]^{2+}$ (Figs. 4f and Fig. S34).

Although the comparison of Au@SiO_2-$[Fe(bpy)_3]^{2+}$ and Au-$[Fe(bpy)_3]^{2+}$ enables preliminarily differentiation of plasmonic charge and energy transfer mechanisms, yet the synergistic effect between these mechanisms still needs to be identified to achieve precise quantification. For this purpose, we further replaced the nanoantenna component in Au-$[Fe(bpy)_3]^{2+}$ with Ag NPs (Fig. S35), whose LSPR occurs at 420 nm and does not sustain spectral overlap with $[Fe(bpy)_3]^{2+}$ for resonant energy transfer[11] (Fig. S36). As the excitation of Ag plasmons and the connection with $[Fe(bpy)_3]^{2+}$ via the thiolated PEG linker could still facilitate plasmonic charge transfer, the Ag-$[Fe(bpy)_3]^{2+}$ control allowed the selective shielding of resonant field-mediated energy transfer mechanisms as well as exclusion of the synergistic, field-mediated charge transport behavior. To exclude the difference between the intrinsic charge carrier-generation efficacy between the Ag and Au nanoantenna, the surface capping of Ag was adjusted to allow for identical surface charge and photocurrent response to the Au antenna (Fig. S37a, b). Identical particle size and $[Fe(bpy)_3]^{2+}$ surface density was also maintained for Ag-$[Fe(bpy)_3]^{2+}$, which led to a slightly reduced photocatalytic performance ($J_{photo} = -21.56$ mA/cm^2) compared to Au-$[Fe(bpy)_3]^{2+}$ (Fig. S37c).

Hence, the contributions from all five possible mechanisms could be feasibly quantified normalized to the photocurrent density obtained from the Au-$[Fe(bpy)_3]^{2+}$ nanoreactor (Figs. 5a, see also Fig. S38). For the hydrogen evolution half reaction and under broad-band Xe lamp illumination, the intrinsic photocatalytic performance of the $[Fe(bpy)_3]^{2+}$ molecules (mechanism (iv)) accounts for a small portion of the total photocurrent, and was quantified by assessing the J_{photo} of an inert silica core-loaded $[Fe(bpy)_3]^{2+}$ at identical loading concentration (Fig. S39). A proportion of 7.6 ± 1.5% was thus calculated (Fig. S40, Eq. S1), and was subtracted from additional contributions (Eq. S2). The contribution of the photothermal effect (mechanism (v)) could be quantified by assessing the current density at 5 °C above room temperature (Eq. S3), which corresponds to the photothermal surface temperature increase according to in-situ Raman nano-thermometry, and a proportion of 15.5 ± 8.4% was calculated (Fig. 5b).

Plasmonic charge carrier-induced photochemistry (mechanism (i)) could be quantified using the J_{photo} of Ag-$[Fe(bpy)_3]^{2+}$ (Eq. S4), which accounts for 57.2 ± 8.4% of the total catalytic performance, and represents a dominant factor to the hydrogen evolution process. This is in line with previous reports that the charge carrier-induced reactivity typically has larger contributions in catalysis of reduction reactions[9,11]. As discussed above, the difference between the photocurrent densities of Au@SiO_2-$[Fe(bpy)_3]^{2+}$ and the intrinsic catalytic properties of $[Fe(bpy)_3]^{2+}$ defines the contribution from resonant energy transfer process (mechanism (ii)) (Eq. S5), for which a mere 0.8 ± 0.1% was calculated. Finally, the difference between Au-$[Fe(bpy)_3]^{2+}$ and Ag-$[Fe(bpy)_3]^{2+}$ represents the contribution from resonant field-enhancement, with the synergistic effect of field-mediated charge transport and photothermal effect included (mechanisms (ii), (iii) and (v)) (Eq. S6). Thus, the synergistic effect between plasmon-mediated energy and charge transfer processes through resonant field-mediated charge separation can be quantified by combining Eqs. S3, S5, S6 (Eq. S7), and is calculated to be 18.9 ± 1.1% (Fig. 5b). These results thus indicate significant contributions by resonant plasmonic near field-facilitated carrier effect.

https://doi.org/10.1038/s41467-025-57569-0

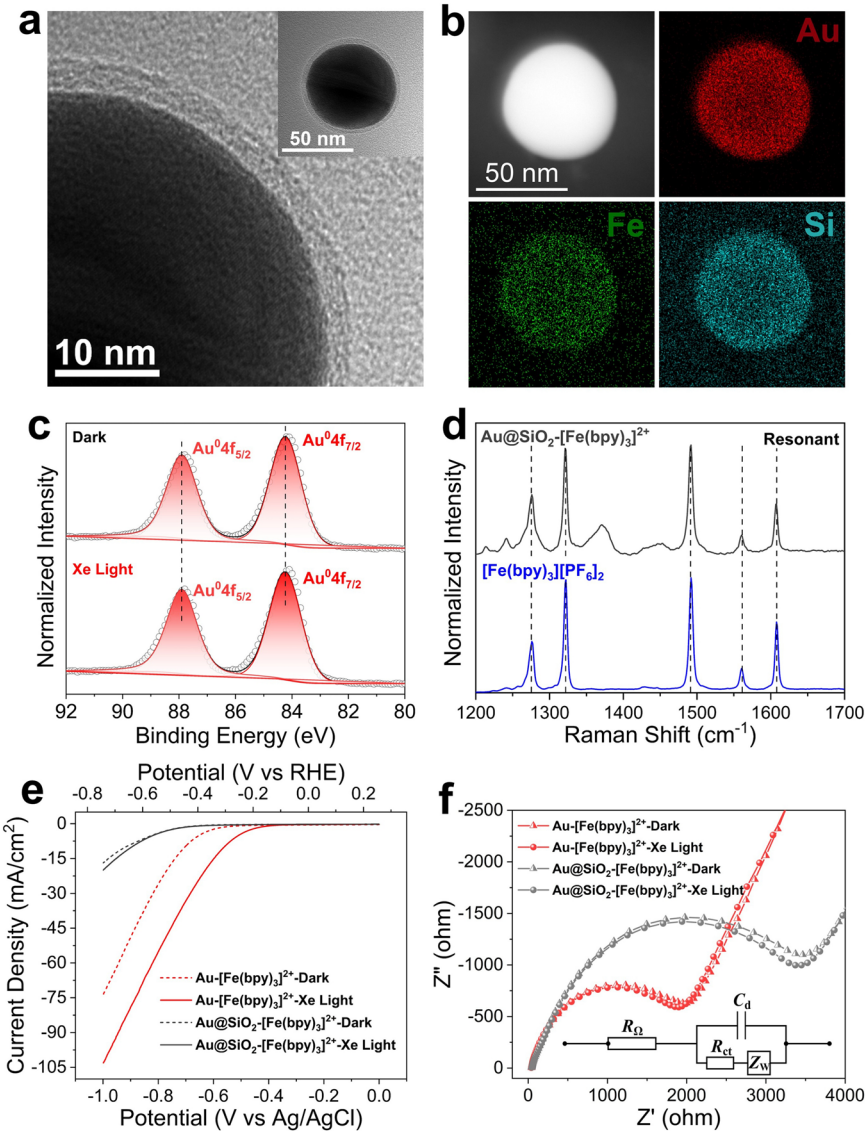

Fig. 4 | Differentiation of resonant plasmonic charge and energy transfer mechanisms. a TEM images and (**b**) STEM and EDS elemental mappings of $Au@SiO_2$-$[Fe(bpy)_3]^{2+}$. **c** Au 4 f *ISI*-XPS spectrum and fittings in dark or under Xe-lamp irradiation for $Au@SiO_2$-$[Fe(bpy)_3]^{2+}$. **d** Raman spectra of $Au@SiO_2$-$[Fe(bpy)_3]^{2+}$ and $[Fe(bpy)_3]^{2+}$ with resonant incident wavelength. **e** LSV curves and (**f**) EIS Nyquist plots of Au-$[Fe(bpy)_3]^{2+}$ and $Au@SiO_2$-$[Fe(bpy)_3]^{2+}$ in dark or upon 1-sun Xe-lamp irradiation.

The selective shielding strategy developed in this work is highly generalized towards distinct catalytic reactions and catalyst configurations. To demonstrate this aspect, we first quantified the contributions of various mechanisms in the oxygen evolution process for Au-$[Fe(bpy)_3]^{2+}$ using the above method (Figs. S41, S42). Notably, the charge transfer effect in Au-$[Fe(bpy)_3]^{2+}$ is found to be unfavorable in the oxidation process (Fig. S23a). Resonant energy transfer-mediated photocatalytic pathway contributes to 53.9 ± 1.6% of the total photocurrent density, representing a dominant factor in the catalysis of oxygen evolution. In contrast, intrinsic catalytic performance of $[Fe(bpy)_3]^{2+}$ accounts for 17.3 ± 0.5%, and photothermal heating-mediated reactivity had a more evident contribution of 28.8 ± 13.6%. These results indicate evident variations in the plasmonic photocatalytic mechanisms under different chemical environments. Furthermore, we have also achieved quantification of distinct mechanisms associated with plasmonic catalysts with (a) different antenna components (Au, Ag NPs), (b) sizes (40, 60 nm), (c) catalyst components ($[Fe(bpy)_3]^{2+}$, cobalt porphyrin, or a CdS semiconductor photocatalyst), and (d) catalyst loadings (Figs. S43, S44). With different catalyst type or loading, the contributions from individual mechanism vary significantly. Particularly, increased contributions from hot carrier-induced photochemistry are recorded using smaller nanoantenna cores, or with lower catalyst loadings (Fig. S43), respectively due to the more efficient carrier extraction and less intermolecular charge hopping behavior[69,70]. In addition, contributions from resonant plasmonic near field-mediated energy transfer to hydrogen evolution photocurrent could be significantly enhanced through the use of Ag nanoantenna and resonant catalyst components including cobalt porphyrin (Ag-CoPTyP) and CdS (Ag@CdS) (Fig. S44), consistent with the augmented near field intensity around Ag nanoantenna[71,72]. These results corroborate the general applicability of our strategy and are particularly helpful for modulating the plasmonic catalytic mechanisms towards distinct fields of applications.

Discussion

In summary, we have developed a highly generalized selective-shielding strategy that differentiates and quantifies the contributions of distinct plasmonic photocatalytic mechanisms, including resonant

https://doi.org/10.1038/s41467-025-57569-0

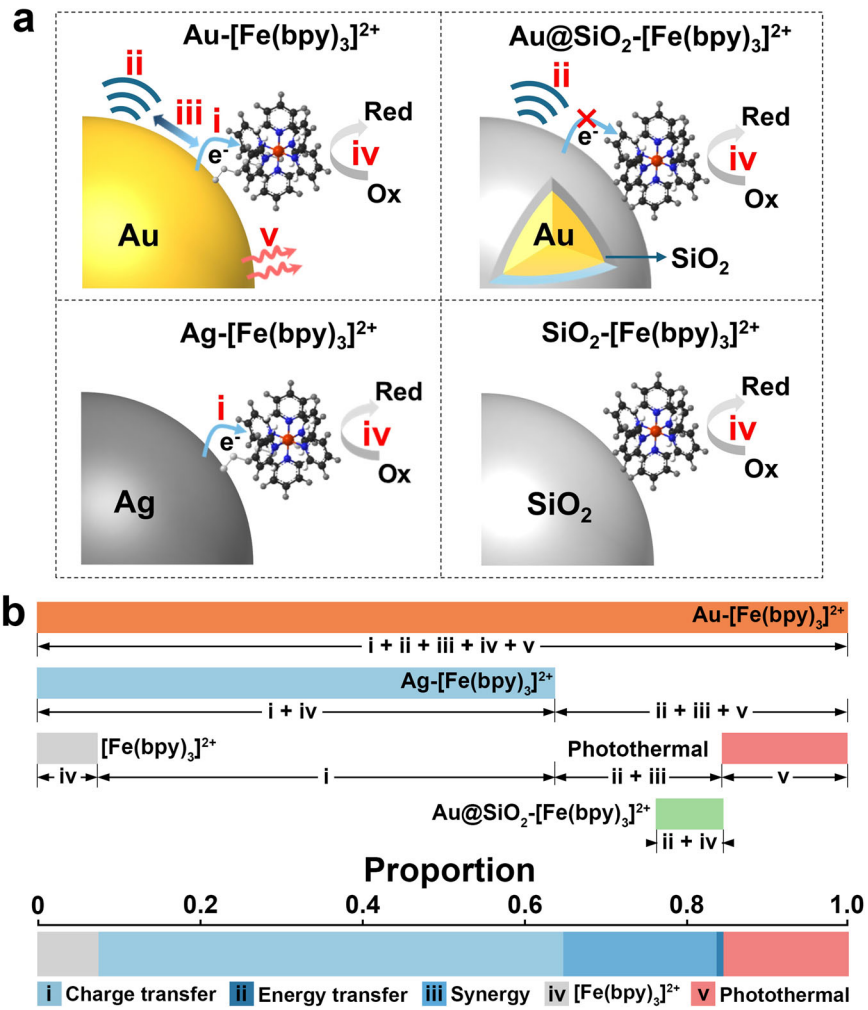

Fig. 5 | Quantification of Distinct Plasmonic Enhancement Mechanisms. **a** Schematic representation of the plasmonic enhancement mechanisms in the Au-$[Fe(bpy)_3]^{2+}$ nanocatalyst and controls. (i)–(v) respectively represent contributions from plasmonic charge carrier-induced photochemistry, resonant energy transfer, synergistic field-mediated charge transfer, intrinsic reactivity of $[Fe(bpy)_3]^{2+}$, and thermal effects. **b** Percentage contribution of distinct plasmonic pathways to hydrogen evolution photocurrent.

near-field-mediated plasmonic energy transfer, hot carrier-induced photochemistry, and photothermal heating-mediated reactivity, using a prototypical Au-$[Fe(bpy)_3]^{2+}$ antenna-reactor photocatalyst. Through modifications of the resonance condition and connection routes, plasmonic charge and energy transfer mechanisms were selectively shielded, allowing for plausible quantification of these mechanisms as well as their synergistic effect. It is found that plasmonic charge carrier-mediated photochemical reactivity dominates the photocurrent (~57%) in a reducing, hydrogen evolution environment, whereas resonant plasmonic energy transfer dominates (~54%) in an oxidative, oxygen evolution environment. Our strategy provides fundamental, quantitative and highly generalized understandings on the role of plasmon resonance in photocatalysis. It also provides important design principles for plasmonic photocatalysts towards distinct reaction types and catalyst configurations.

Methods

Preparation of Au-$[Fe(bpy)_3]^{2+}$ plasmonic nanocatalyst

First, the synthesized Au colloid was thoroughly washed with DI water three times to remove PVP. Then, HS-PEG-COOH aqueous solution (1 mg/mL, 1 mL) and $[Fe(bpy)_3]^{2+}$ solution (1:1 ratio of water to ethanol, 4.6 mg/mL, 150 μL) were added, after stirring for 12 h under dark condition, it was washed twice with DI water to obtain Au-$[Fe(bpy)_3]^{2+}$.

Preparation of Au@SiO_2-$[Fe(bpy)_3]^{2+}$ and Ag-$[Fe(bpy)_3]^{2+}$ controls

Au@SiO_2-$[Fe(bpy)_3]^{2+}$ was obtained by mixing the synthesized Au@SiO_2 colloid (1 mL) with $[Fe(bpy)_3]^{2+}$ solution (1:1 ratio of water to ethanol, 4.6 mg/mL, 140 μL) and stirring for 3 h, the $[Fe(bpy)_3]^{2+}$ molecules are attached to negatively charged SiO_2 surface through electrostatic interaction, and then washed three times with DI water. For the preparation of Ag-$[Fe(bpy)_3]^{2+}$, dispersed 0.5 mg of Ag NPs in HS-PEG-COOH aqueous solution (1 mg/mL, 1 mL), then added 150 μL of $[Fe(bpy)_3]^{2+}$ solution (1:1 ratio of water to ethanol, 4.6 mg/mL) and stirred for 12 h under dark condition, it was washed twice with DI water to obtain Ag-$[Fe(bpy)_3]^{2+}$. The Fe concentrations in Au-$[Fe(bpy)_3]^{2+}$, Au@SiO_2-$[Fe(bpy)_3]^{2+}$ and Ag-$[Fe(bpy)_3]^{2+}$ and remain consistent according to the ICP-OES results.

Measurement of Raman spectroscopy

The in-text Raman spectra and maps of different samples were measured on drop-casted thin films of Au-$[Fe(bpy)_3]^{2+}$ and controls on silicon wafer substrates (⟨100⟩, Ferrotec Shanghai) or in an in-situ electrolysis cell with the Renishaw InVia confocal Raman Microscope with 100× air objective (Leica, Numerical Aperture = 1.25). Excitation laser of 532 nm (1800 l/mm diffraction grating), 633 nm (1800 l/mm diffraction grating), and 785 nm (1200 l/mm diffraction grating) were used with 0.5% laser powers and 10 s exposure time.

Measurement of single-particle scattering spectroscopy

Scattered light was collected with a 50× air-spaced objective (Zeiss, NA = 0.8) and passed to a hyperspectral detection system consisting of an imaging spectrograph with a slit aperture (Princeton Instrument, Acton SpectraPro 2156) coupled to a thermoelectrically cooled back-illuminated CCD camera (Princeton Instrument, Pixis 400BR) and mounted on a computer-controlled translation stage (Newport, LTA-HL).

In Situ X-ray absorption fine structure (XAFS) characterization

XAFS spectroscopy at the Fe K-edge was performed on sector 20 BM-B of APS, equipped with an external xenon light source. All samples were ground lightly using a mortar and pestle. The powder was dispersed onto Kapton tape, forming a uniform and homogeneous layer, which was then folded a few times to achieve absorption of at least 20%. Fe K-edge XAFS spectra of Au-$[Fe(bpy)_3]^{2+}$ and $[Fe(bpy)_3](PF_6)_2$ were recorded in transmission mode by measuring the incident and transmitted photon flux in ionization chambers I_0 and I_t, respectively. Standard Fe foil was used as reference for beamline energy calibration at the Fe K-edge. The background removal, normalization and Fourier transform (FT) of XAFS spectra were performed using Athena software. The extracted EXAFS data were weighted by k^3 and then converted to R space by FT to obtain the magnitude plots of the EXAFS spectra.

In situ XPS characterization (ISI-XPS)

X-ray photoelectron spectroscopy was performed on XPS Thermo Escalab 250Xi. During the experimental process, full-spectrum light source with the light intensity of 100 mW/cm^2 (HF-GHX-XE-300) were used as the illumination source. The light irradiation was introduced into the analysis chamber through the quartz window, which allowed illumination from the top. Then, the spectra of Au 4 f and Fe 2p were analyzed in dark and under light conditions to investigate the behavior of electron transfer.

Reporting summary

Further information on research design is available in the Nature Portfolio Reporting Summary linked to this article.

Data availability

The data related to the figures in the paper are provided as Excel files in Source data. Source data are provided with this paper.

References

1. Zhou, L. A. et al. Quantifying hot carrier and thermal contributions in plasmonic photocatalysis. *Science* **362**, 69–72 (2018).
2. Yuan, Y. G. et al. Earth-abundant photocatalyst for H_2 generation from NH_3 with light-emitting diode illumination. *Science* **378**, 889–893 (2022).
3. Linic, S., Christopher, P. & Ingram, D. B. Plasmonic-metal nanostructures for efficient conversion of solar to chemical energy. *Nat. Mater.* **10**, 911–921 (2011).
4. Li, J. et al. Plasmon-induced resonance energy transfer for solar energy conversion. *Nat. Photonics* **9**, 601–607 (2015).
5. Saavedra, J. et al. Controlling activity and selectivity using water in the Au-catalysed preferential oxidation of CO in H_2. *Nat. Chem.* **8**, 584–589 (2016).
6. Aslam, U., Rao, V. G., Chavez, S. & Linic, S. Catalytic conversion of solar to chemical energy on plasmonic metal nanostructures. *Nat. Catal.* **1**, 656–665 (2018).
7. Yang, J., Guo, Y., Lu, W., Jiang, R. & Wang, J. Emerging applications of plasmons in driving CO_2 reduction and N_2 fixation. *Adv. Mater.* **30**, 1802227 (2018).
8. Hu, C. et al. Near-infrared-featured broadband CO_2 reduction with water to hydrocarbons by surface plasmon. *Nat. Commun.* **14**, 221 (2023).
9. Ingram, D. B. & Linic, S. Water splitting on composite plasmonic-metal/semiconductor photoelectrodes: evidence for selective plasmon-induced formation of charge carriers near the semiconductor surface. *J. Am. Chem. Soc.* **133**, 5202–5205 (2011).
10. Fan, W. et al. Photosensitive polymer and semiconductors bridged by Au plasmon for photoelectrochemical water splitting. *Appl. Catal. B* **195**, 9–15 (2016).
11. An, X., Stelter, D., Keyes, T. & Reinhard, B. M. Plasmonic photocatalysis of urea oxidation and visible-light fuel cells. *Chem* **5**, 2228–2242 (2019).
12. Huang, L. et al. Synergy between plasmonic and electrocatalytic activation of methanol oxidation on palladium-silver alloy nanotubes. *Angew. Chem. Int. Ed. Engl.* **58**, 8794–8798 (2019).
13. Li, Z. et al. Photo-driven hydrogen production from methanol and water using plasmonic cu nanoparticles derived from layered double hydroxides. *Adv. Funct. Mater.* **33**, 2213672 (2022).
14. Li, S. et al. Recent advances in plasmonic nanostructures for enhanced photocatalysis and electrocatalysis. *Adv. Mater.* **33**, e2000086 (2021).
15. Zhan, C., Moskovits, M. & Tian, Z.-Q. Recent progress and prospects in plasmon-mediated chemical reaction. *Matter* **3**, 42–56 (2020).
16. Ren, H. et al. Core–shell–satellite plasmonic photocatalyst for broad-spectrum photocatalytic water splitting. *ACS Mater. Lett.* **3**, 69–76 (2020).
17. Zhu, Z., Tang, R., Li, C., An, X. & He, L. Promises of plasmonic antenna-reactor systems in gas-phase CO_2 photocatalysis. *Adv. Sci.* **10**, e2302568 (2023).
18. Kale, M. J., Avanesian, T. & Christopher, P. Direct photocatalysis by plasmonic nanostructures. *ACS Catal.* **4**, 116–128 (2013).
19. An, X. et al. Wavelength-dependent bifunctional plasmonic photocatalysis in au/chalcopyrite hybrid nanostructures. *ACS Nano* **16**, 6813–6824 (2022).
20. Choi, K. M. et al. Plasmon-enhanced photocatalytic CO_2 conversion within metal-organic frameworks under visible light. *J. Am. Chem. Soc.* **139**, 356–362 (2017).
21. Shi, R. et al. Self-assembled Au/CdSe nanocrystal clusters for plasmon-mediated photocatalytic hydrogen evolution. *Adv. Mater.* **29**, 1700803 (2017).
22. Chen, X., Zhu, H. Y., Zhao, J. C., Zheng, Z. F. & Gao, X. P. Visible-light-driven oxidation of organic contaminants in air with gold nanoparticle catalysts on oxide supports. *Angew. Chem. Int. Ed. Engl.* **47**, 5353–5356 (2008).
23. Lin, W. & Murphy, C. J. A demonstration of Le Chatelier's principle on the nanoscale. *ACS Cent. Sci.* **3**, 1096–1102 (2017).
24. Linic, S., Chavez, S. & Elias, R. Flow and extraction of energy and charge carriers in hybrid plasmonic nanostructures. *Nat. Mater.* **20**, 916–924 (2021).
25. Elias, R. C. & Linic, S. Elucidating the roles of local and nonlocal rate enhancement mechanisms in plasmonic catalysis. *J. Am. Chem. Soc.* **144**, 19990–19998 (2022).
26. Dubi, Y., Un, I. W., Baraban, J. H. & Sivan, Y. Distinguishing thermal from non-thermal contributions to plasmonic hydrodefluorination. *Nat. Catal.* **5**, 244–246 (2022).
27. Robatjazi, H. et al. Plasmon-induced selective carbon dioxide conversion on earth-abundant aluminum-cuprous oxide antenna-reactor nanoparticles. *Nat. Commun.* **8**, 27 (2017).
28. Robatjazi, H. et al. Plasmon-driven carbon–fluorine ($C(sp^3)$–F) bond activation with mechanistic insights into hot-carrier-mediated pathways. *Nat. Catal.* **3**, 564–573 (2020).
29. Zhou, L. et al. Light-driven methane dry reforming with single atomic site antenna-reactor plasmonic photocatalysts. *Nat. Energy* **5**, 61–70 (2020).
30. Cushing, S. K. et al. Photocatalytic activity enhanced by plasmonic resonant energy transfer from metal to semiconductor. *J. Am. Chem. Soc.* **134**, 15033–15041 (2012).

31. Zhang, Y. et al. Surface-plasmon-driven hot electron photochemistry. *Chem. Rev.* **118**, 2927–2954 (2017).
32. Larsen, A. G., Holm, A. H., Roberson, M. & Daasbjerg, K. Substituent effects on the oxidation and reduction potentials of phenylthiyl radicals in acetonitrile. *J. Am. Chem. Soc.* **123**, 1723–1729 (2001).
33. Mosquera, J. et al. Plasmonic nanoparticles with supramolecular recognition. *Adv. Funct. Mater.* **30**, 1902082 (2020).
34. Mori, K., Kawashima, M., Che, M. & Yamashita, H. Enhancement of the photoinduced oxidation activity of a ruthenium(ii) complex anchored on silica-coated silver nanoparticles by localized surface plasmon resonance. *Angew. Chem. Int. Ed. Engl.* **49**, 8598–8601 (2010).
35. Tian, S., Gao, W., Liu, Y., Kang, W. & Yang, H. Effects of surface modification Nano-SiO_2 and its combination with surfactant on interfacial tension and emulsion stability. *Colloids Surf.* **595**, 124682 (2020).
36. Liu, Y. et al. Tailored surface wettability and pore structure of hydrophobic SiO2/SiC membranes for preparing monodisperse emulsion with high-efficiency. *Appl. Surf. Sci.* **665**, 165364 (2024).
37. Ma, Z. et al. TCR triggering by pMHC ligands tethered on surfaces via poly(ethylene glycol) depends on polymer length. *PLoS One* **9**, e112292 (2014).
38. Alexander, B. D., Dines, T. J. & Longhurst, R. W. DFT calculations of the structures and vibrational spectra of the $[Fe(bpy)_3]^{2+}$ and $[Ru(bpy)_3]^{2+}$ complexes. *Chem. Phys.* **352**, 19–27 (2008).
39. Behera, M. & Ram, S. Mechanism of solubilizing fullerene C60in presence of poly(vinyl pyrrolidone) molecules in water. *Fuller. Nanotub. Carbon Nanostruct.* **23**, 906–916 (2015).
40. Sylvestre, J.-P. et al. Surface chemistry of gold nanoparticles produced by laser ablation in aqueous media. *J. Phys. Chem. B* **108**, 16864–16869 (2004).
41. Casaletto, M. P., Longo, A., Martorana, A., Prestianni, A. & Venezia, A. M. XPS study of supported gold catalysts: the role of Au^0 and $Au^{+\delta}$ species as active sites. *Surf. Interface Anal.* **38**, 215–218 (2006).
42. Li, X., Zhu, J. & Wei, B. Hybrid nanostructures of metal/two-dimensional nanomaterials for plasmon-enhanced applications. *Chem. Soc. Rev.* **45**, 3145–3187 (2016).
43. Liz-Marzan, L. M., Murphy, C. J. & Wang, J. Nanoplasmonics. *Chem. Soc. Rev.* **43**, 3820–3822 (2014).
44. Li, S., Dong, K., Cai, M., Li, X. & Chen, X. A plasmonic S-scheme Au/MIL-101(Fe)/BiOBr photocatalyst for efficient synchronous decontamination of Cr(VI) and norfloxacin antibiotic. *eScience* **4**, 100208 (2024).
45. Slaughter, L. S., Wu, Y. P., Willingham, B. A., Nordlander, P. & Link, S. Effects of symmetry breaking and conductive contact on the plasmon coupling in gold nanorod dimers. *ACS Nano* **4**, 4657–4666 (2010).
46. Hoggard, A. et al. Using the plasmon linewidth to calculate the time and efficiency of electron transfer between gold nanorods and graphene. *ACS Nano* **7**, 11209–11217 (2013).
47. Lerch, S. & Reinhard, B. M. Effect of interstitial palladium on plasmon-driven charge transfer in nanoparticle dimers. *Nat. Commun.* **9**, 1608 (2018).
48. Sun, S. et al. All-Dielectric Full-Color Printing with TiO_2 Metasurfaces. *ACS Nano* **11**, 4445–4452 (2017).
49. Fatur, S. M., Shepard, S. G., Higgins, R. F., Shores, M. P. & Damrauer, N. H. A Synthetically tunable system to control MLCT excited-state lifetimes and spin states in iron(ii) polypyridines. *J. Am. Chem. Soc.* **139**, 4493–4505 (2017).
50. Aubock, G. & Chergui, M. Sub-50-fs photoinduced spin crossover in $[Fe(bpy)_3]^{2+}$. *Nat. Chem.* **7**, 629–633 (2015).
51. Hung, T. C. et al. Activating the fluorescence of a Ni(II) complex by energy transfer. *J. Am. Chem. Soc.* **146**, 8858–8864 (2024).
52. Cao, S.-W. et al. Solar-to-fuels conversion over In_2O_3/g-C_3N_4 hybrid photocatalysts. *Appl. Catal. B* **147**, 940–946 (2014).
53. Zhang, C. et al. Modulating the plasmon-mediated oxidation of p-aminothiophenol with asymmetrically grafted thiol molecules. *J. Phys. Chem. Lett.* **11**, 7650–7656 (2020).
54. Dey, A. et al. Hydrogen evolution with hot electrons on a plasmonic-molecular catalyst hybrid system. *Nat. Commun.* **15**, 445 (2024).
55. Sheng, H. et al. Strong synergy between gold nanoparticles and cobalt porphyrin induces highly efficient photocatalytic hydrogen evolution. *Nat. Commun.* **14**, 1528 (2023).
56. Dey, A. et al. Exploiting hot electrons from a plasmon nanohybrid system for the photoelectroreduction of CO_2. *Commun. Chem.* **7**, 59 (2024).
57. Ly, N. H., Vasseghian, Y. & Joo, S.-W. Plasmonic photocatalysts for enhanced solar hydrogen production: A comprehensive review. *Fuel* **344**, 128087 (2023).
58. Zhang, C., Zhao, G., Zhang, D., Wang, S. & Sun, W. Two-dimensional germanium for photocatalysis. *Inf. Funct. Mater.* **1**, 108–123 (2024).
59. Ryu, J. et al. Thermochemical aerobic oxidation catalysis in water can be analysed as two coupled electrochemical half-reactions. *Nat. Catal.* **4**, 742–752 (2021).
60. Zhan, C. et al. Disentangling charge carrier from photothermal effects in plasmonic metal nanostructures. *Nat. Commun.* **10**, 2671 (2019).
61. Ou, W. et al. Thermal and nonthermal effects in plasmon-mediated electrochemistry at nanostructured ag electrodes. *Angew. Chem. Int. Ed. Engl.* **59**, 6790–6793 (2020).
62. Seker, P. et al. Decoupling plasmonic hot carrier from thermal catalysis via electrode engineering. *Nano Lett.* **24**, 8619–8625 (2024).
63. Li, H. et al. Plasmon-induced local electric field improved hydrogen evolution reaction on Ag/Mo2C nanosheets. *Nano Res* **18**, 94907146 (2025).
64. Christopher, P., Xin, H. & Linic, S. Visible-light-enhanced catalytic oxidation reactions on plasmonic silver nanostructures. *Nat. Chem.* **3**, 467–472 (2011).
65. Brongersma, M. L., Halas, N. J. & Nordlander, P. Plasmon-induced hot carrier science and technology. *Nat. Nanotechnol.* **10**, 25–34 (2015).
66. Christopher, P., Xin, H., Marimuthu, A. & Linic, S. Singular characteristics and unique chemical bond activation mechanisms of photocatalytic reactions on plasmonic nanostructures. *Nat. Mater.* **11**, 1044–1050 (2012).
67. Elias, R. C., Yan, B. & Linic, S. Probing spatial energy flow in plasmonic catalysts from charge excitation to heating: non-homogeneous energy distribution as a fundamental feature of plasmonic chemistry. *J. Am. Chem. Soc.* **146**, 29656–29663 (2024).
68. Yang, J., Li, L., Xiao, C. & Xie, Y. Dual-plasmon resonance coupling promoting directional photosynthesis of nitrate from air. *Angew. Chem. Int. Ed. Engl.* **62**, e202311911 (2023).
69. Hu, K. & Meyer, G. J. Lateral intermolecular self-exchange reactions for hole and energy transport on mesoporous metal oxide thin films. *Langmuir* **31**, 11164–11178 (2015).
70. DiMarco, B. N. et al. A distance dependence to lateral self-exchange across nanocrystalline TiO_2. a comparative study of three homologous $Ru^{III/II}$ polypyridyl compounds. *J. Phys. Chem. C.* **120**, 14226–14235 (2016).
71. Petrikaitė, V. et al. Stability and SERS signal strength of laser-generated gold, silver, and bimetallic nanoparticles at different KCl concentrations. *Heliyon* **10**, e34815 (2024).
72. McCourt, L. R., Ruppert, M. G., Routley, B. S., Indirathankam, S. C. & Fleming, A. F. A comparison of gold and silver nanocones and geometry optimisation for tip-enhanced microscopy. *J. Raman Spectrosc.* **51**, 2208–2216 (2020).

Acknowledgements
We acknowledge the support from the National Natural Science Foundation of China (W2412063 L.H., 22302137 X.A., 52172221 L.H., 52272229 C.L., 52302297 Z.W., 52402296 Z.Z.), the National Key R&D Program of China (2024YFA1509300 X.A. and C.L., 2021YFF0502000 L.H.), Jiangsu Key Laboratory for Carbon-Based Functional Materials and Devices (ZZ2201), Collaborative Innovation Center of Suzhou Nano Science & Technology and Suzhou Key Laboratory of Advanced Photonics Materials. This research was funded in part by the Austrian Science Fund (FWF) [10.55776/COE5, G.R.] (Cluster of Excellence Materials for Energy Conversion and Storage, MECS). For open-access purposes, the author has applied a CC BY public copyright license to any author-accepted article version arising from this submission. The authors thank Prof. Björn M. Reinhard for helpful discussions on the plasmon-enhancement mechanisms, and Prof. Arkady Yartsev for discussions on dynamics of transition metal complexes.

Author contributions
L.H., X.A., and C.L. conceived and directed the study; S.L., Z.W. and Z.Z. carried out the preparation of materials; S.L. and X.D. carried out the photoelectrochemical measurements; Y.Z. and K.F. performed the FDTD simulation; X. H. and B.W. performed TA spectra measurements; B.Y. and K.N. performed ISI-XPS experiments. Z.W. and J.S. performed XRD and H_2 production measurements. B.Z. and Q.Z. performed Single-particle Scattering Spectroscopy (SCA) experiments; J.W., Y.J., and J.H. conducted the TEM characterization; Y.M. and X. H. carried out the Zeta potential characterization. A.G., Y.Z., and X.A. conducted the simulations; G.R. and X.Z. supervised result analyzes; X.A. and L.H. co-wrote the manuscript with contributions from all the authors.

Competing interests
The Authors declare the following competing interests: L.H., X.A., S.L., and C.L. have filed a patent about the design and fabrication of the Au-$[Fe(bpy)_3]^{2+}$ plasmonic nanocatalyst. All remaining Authors declare no competing interests.

Additional information
Supplementary information The online version contains supplementary material available at https://doi.org/10.1038/s41467-025-57569-0.

Correspondence and requests for materials should be addressed to Chaoran Li, Xingda An or Le He.

Peer review information *Nature Communications* thanks Jacinto Sa and the other, anonymous, reviewer(s) for their contribution to the peer review of this work. A peer review file is available.